

Toward a Geometrical Understanding of Self-supervised Contrastive Learning

Romain Cosentino

*Ming Hsieh Department of Electrical and Computer Engineering
University of Southern California*

rom.cosentino@gmail.com

Anirvan Sengupta

Flatiron Institute & Rutgers University

anirvans.physics@gmail.com

Salman Avestimehr

*Ming Hsieh Department of Electrical and Computer Engineering
University of Southern California*

avestime@usc.edu

Mahdi Soltanolkotabi

*Ming Hsieh Department of Electrical and Computer Engineering
University of Southern California*

msoltoon@gmail.com

Antonio Ortega

*Ming Hsieh Department of Electrical and Computer Engineering
University of Southern California*

aortega@usc.edu

Ted Willke

Intel Labs

ted.willke@intel.com

Mariano Tepper

Intel Labs

mariano.tepper@intel.com

Abstract

Self-supervised learning (SSL) is currently one of the premier techniques to create data representations that are actionable for transfer learning in the absence of human annotations. Despite their success, the underlying geometry of these representations remains elusive, which obfuscates the quest for more robust, trustworthy, and interpretable models. In particular, mainstream SSL techniques rely on a specific deep neural network architecture with two cascaded neural networks: the encoder and the projector. When used for transfer learning, the projector is discarded since empirical results show that its representation generalizes more poorly than the encoder's. In this paper, we investigate the representation induced by the encoder and how the strength of the data augmentation policies as well as the width and depth of the projector affect its representation. We discover a non-trivial relation between the encoder, the projector, and the data augmentation strength: with increasingly larger augmentation policies, the projector, rather than the encoder, is more strongly driven to become invariant to the augmentations. It does so by eliminating crucial information about the data by learning to project it into a low-dimensional space, a noisy estimate of the data manifold tangent plane in the encoder representation. This analysis is substantiated through a geometrical perspective with theoretical and empirical results.

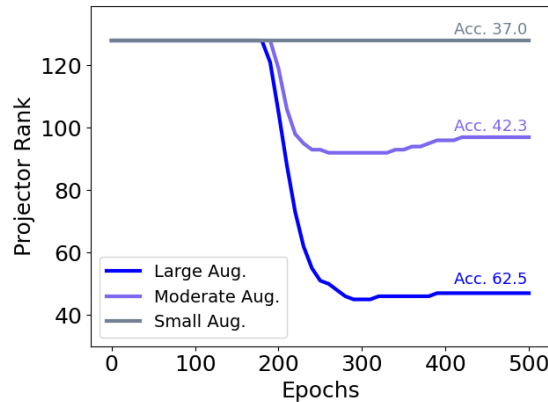


Figure 1: **Evolution throughout contrastive SSL training of the rank of a linear projector of dimension 512×128 for different augmentation strengths, and the associated accuracy obtained on Cifar100 by using the representation extracted in the encoder space.** Large, moderate, and small augmentations refer to the strength of the data augmentation applied to the input samples (see Table 2 for each configuration). The smaller the strength of the data augmentation policy, the less the projector suffers from dimensional collapse. However, when the projector is affected by a substantial dimensional collapse, the encoder representation becomes suitable for the downstream task. In this work, we demystify this intriguing relationship between augmentation strengths, encoder embedding, and projector geometry.

1 Introduction

Training of models that are capable of extracting meaningful data embedding without relying on labels has recently reached new heights with the substantial development of self-supervised learning (SSL) methods. These approaches replace labels required for supervised learning with augmentation policies, which will define the desired invariances of the trained representation. From these augmentation policies, multiple transformed instances of the same sample are generated, and the network is trained so that their embeddings coincide. After training, the network can be used as a mapping for other datasets to obtain an efficient data representation for various downstream tasks. Most of the SSL algorithms developed have shown competitive performances with supervised learning methods Caron et al. (2021); Chen et al. (2020c;b); Grill et al. (2020); Misra & van der Maaten (2019a); Dwibedi et al. (2021a); Bardes et al. (2021); Zbontar et al. (2021); Misra & van der Maaten (2019a); Caron et al. (2018); Li et al. (2020); Tian et al. (2020); Grill et al. (2020); Caron et al. (2021), and more importantly, are more efficient to perform transfer learning for most data distributions and tasks Ericsson et al. (2020); Caron et al. (2021).

While the generalization capability of SSL models has been observed empirically, their inner functioning and the key components to their success remain elusive. Recently, researchers have attempted to capture an understanding of SSL paradigm; In HaoChen et al. (2021), they provide a graph formulation of contrastive loss functions and leverage it to provide generalization guarantees. The authors in Jing et al. (2021) analyzes contrastive loss functions and the dimensional collapse problem based on the gradient of a linear network. Similarly, Wang & Isola (2020) analyzes theoretically an end-to-end network mapping the input to output living on the unit sphere and fed into the constrastive loss function. In Huang et al. (2021) they consider a distance-based theoretical approach to highlight the importance of the data augmentations in constastive SSL. Another line of work, Wang & Liu (2021), considers the impact of the temperature parameter used in SSL loss function and how it impacts the data embedding. Another approach considers non-contrastive loss function and performs a spectral analysis of DNN’s mapping Tian et al. (2021).

Interestingly, most SSL frameworks developed so far do not use the data embedding provided by the entire trained network’s output and instead use the representation extracted from an internal layer. In particular, the deep neural network (DNN) that is used for SSL is usually composed of two cascaded neural networks: the encoder (backbone) and the projector. Usually, the encoder is a residual network, or more recently, a

vision transformer, and the projector is an MLP. While the projector output is used for training, only the encoder representation is used for downstream tasks. It is known that the representation at the output of the projector, which is designed to be almost invariant to the selected augmentations, discards crucial features for downstream tasks, such as color, rotation, and shape, while the one at the output of the encoder still contains these features Chen et al. (2020b); Appalaraju et al. (2020).

While the work developed so far aiming at understand the behaviour of SSL provide insights into its various aspects, none of them describe the embedding that is used for downstream task: the encoder’s output. Their theoretical modelisation of SSL paradigm consider the output of the projector. To open the door to the understanding of the transfer learning capability of DNN trained in a SSL regime, it is crucial to take into account this structural specificity. In this work, we propose to capture *the behaviour of the encoder’s network* from a geometrical point of view. In particular our approach aims at demystifying the observation depicted in Fig. 1, where we display the evolution of the rank of weights of a linear projector during training. We observe that there is an interplay between the *generalization capability* of the encoder’s representation, the *strength* of the augmentations, and the *rank collapse* of the weights of the projector. In our study, we take a geometrical approach to understand this relationship as well as the benefits on the encoder’s representation of using a non-linear projector. Our contribution can be summarized as follows:

- **Interpretable InfoNCE upper bound.** We first derive an interpretable upper bound of the InfoNCE loss function van den Oord et al. (2019), a vastly used loss in SSL. This upper bound is then leveraged throughout the paper to derive insights into the geometry of SSL algorithms (Sec. 3).
- **Dimensional collapse of the projector and data augmentation strength.** We show that the dimensional collapse of the projector depends on (i) the per-sample augmentation strength, (ii) the number of augmentations. We also show how they affect the distribution of the data in the encoder’s output space. To do so, we theoretically analyze two forces driving the InfoNCE loss function: undoing the effect of the data augmentation policies and reducing the similarity between each datum and its negative samples (Sec. 4).
- **Impact of data augmentation strength, depth and width of projector onto encoder’s representation.** We show that there exists an intricate relationship between the estimation of the data manifold tangent space performed by the encoder and the strength of the augmentations. In particular, (i) in the case of large augmentations, the estimate of the data manifold tangent space at initialization is poor, but, as training progresses augmentations become beneficial for representing data manifold directions more accurately, (ii) in the case of small augmentations the estimation of the data manifold tangent plane remains poor throughout the training. We also show that with a linear projector, the encoder is constrained to project the data manifold onto a linear subspace, while a non-linear projector enables the encoder to map the tangent space of the data manifold onto a continuous and piecewise affine subspace, therefore unlocking its expressive capability (Sec. 5).

2 Background and notations

Notations. We will denote by $(\mathbf{x}_i)_{i=1}^N$, the original data in \mathbb{R}^d , $\mathbf{x}_i^{(1)} = t_1(\mathbf{x}_i)$, $t_1 \sim \mathcal{T}$ and $\mathbf{x}_i^{(2)} = t_2(\mathbf{x}_i)$, $t_2 \sim \mathcal{T}$ the augmented pairs obtained by sampling a distribution of augmentation, \mathcal{T} , and applying the sampled transformation onto each input data. These augmented pairs are fed into the network $f = g \circ h$ where h is the encoder with output dimension d_{enc} and g the projector with output dimension d_{proj} . Notations are summarized in Table 1.

Architecture and hyperparameters. For all the experiments performed in this work, we used the SimCLR framework Chen et al. (2020b), trained using the InfoNCE loss function. The encoder is

Table 1: Notation reference card

$\mathbf{x}_i \in \mathbb{R}^d$	input data
\mathcal{T}	augmentation distribution
$\mathbf{x}_i^{(k)} \in \mathbb{R}^d, k = 1, 2$	augmented pair
$h : \mathbb{R}^d \rightarrow \mathbb{R}^{d_{\text{enc}}}$	encoder mapping
$g : \mathbb{R}^{d_{\text{enc}}} \rightarrow \mathbb{R}^{d_{\text{proj}}}$	projector mapping
$f = g \circ h : \mathbb{R}^d \rightarrow \mathbb{R}^{d_{\text{proj}}}$	encoder and projector mapping
$\mathbf{f}_i^{(k)} = \mathbf{g}_i^{(k)} \circ \mathbf{h}_i^{(k)}$	$f(\mathbf{x}_i^{(k)}) = g(\mathbf{x}_i^{(k)}) \circ h(\mathbf{x}_i^{(k)})$
W	linear projector’s weights
B_{-i}	$\{(j, k) j \neq i, k = 1, 2\}$
$\{\tilde{\mathbf{f}}_l, l \in B_{-i}\}$	$\{\mathbf{f}_j^{(k)} j \neq i, k = 1, 2\}$
$\tilde{\mathbf{h}}_i^*$	$\arg \max_{\tilde{\mathbf{h}}_l, l \in B_{-i}} \mathbf{h}_i^{(1)T} W W^T \tilde{\mathbf{h}}_l$
$\delta \mathbf{h}_i$	$\mathbf{h}_i^{(2)} - \mathbf{h}_i^*$
S	$\text{Span}\{\delta \mathbf{h}_i, i = 1, \dots, N\}$
$\text{Proj}(\mathbf{h}_i^{(1)})$	$W W^T \mathbf{h}_i^{(1)}$

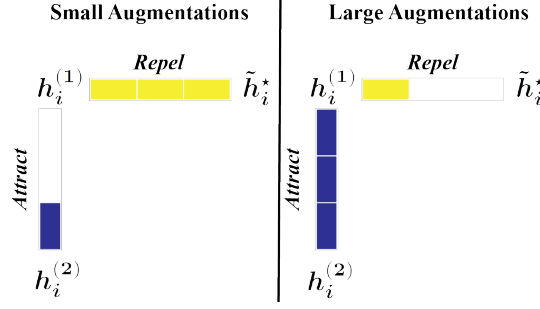


Figure 2: **The strength of the augmentations (depicted as “power bars”) acts as a weighting term balancing the attraction of augmented samples and the repulsion effect of the negative samples.** Contrastive SSL introduces negative samples to avoid feature collapse, which aims at enforcing the representation learned to fill the available dimensions. Under the InfoNCE loss, Eq. (1), there is a trade-off between the repulsion effect induced by the negative samples and the invariance property enforced by maximizing the similarity between two augmented versions of the same sample. We show that the strength of the data augmentation policies acts as a per-datum weight reinforcing the invariance term and reducing the effect of the negative samples. On the contrary, reducing the strength of the augmentations accentuates the repulsing effect from the negative samples. (Notations detailed in Table 1).

defined as a Resnet18 with output dimension $d_{\text{enc}} = 512$. The projector is linear with output dimension $d_{\text{proj}} = 128$. The optimization of the loss function is performed using LARS You et al. (2017) with learning rate 4.0, weight decay 10^{-6} , and momentum 0.9. The dataset under consideration is Cifar100 Krizhevsky et al. (2009), sensible tradeoff between the computational resources needed for training and the challenge it poses to Resnet18 (i.e., to avoid fitting it with too much ease).

Data augmentation policies. The augmentation policies to train SimCLR as well as to perform our analysis will be based on: random horizontal flipping, random resized crop, random color jittering, and random grayscale (see <https://pytorch.org/vision/stable/transforms.html> for details). Three settings will be tested: small augmentations, moderate augmentations, and large augmentations. The details of the hyperparameters are shown in Table 2, where for resized crop, we display the scale parameter, and for color jittering the parameter s that such that brightness $(0.8s)$, contrast $(0.8s)$, saturation $(0.8s)$, and hue $(0.2s)$. Note that the large augmentation setting corresponds to the optimal parameters to obtain the best representation on Cifar100.

Table 2: Data Augmentation Policies

	Augmentation strength		
	Large	Moderate	Small
Horiz. flipping	✓	✓	✗
Grayscale (p = 0.2)	✓	✓	✓
Resized crop	0.08 – 1	0.5 – 1	0.9 – 1
Color jittering (p = 0.8)	s = 0.5	s = 0.25	s = 0.05

Loss function. The infoNCE loss function, widely used in contrastive learning Chen et al. (2020a;c); Misra & van der Maaten (2019b); He et al. (2020); Dwibedi et al. (2021b); Yeh et al. (2021) is defined as

$$\mathcal{L}_{\text{infoNCE}} = -\frac{1}{N} \sum_{i=1}^N \log \left(\frac{\exp(\beta \mathbf{f}_i^{(1)T} \mathbf{f}_i^{(2)})}{\sum_{l \in B_{-i}} \exp(\beta \mathbf{f}_i^{(1)T} \tilde{\mathbf{f}}_l)} \right), \quad (1)$$

where $\{\tilde{\mathbf{f}}_l : l \in B_{-i}\} = \{\mathbf{f}_j^{(k)} : j \neq i, k = 1, 2\}$. Thus, for each i , B_{-i} consists of the indices of the negative samples related to \mathbf{x}_i , i.e., all the data points except the two augmentations $\mathbf{x}_i^{(1)}$ and $\mathbf{x}_i^{(2)}$. Note that all projector outputs are normalized, that is, $\|\mathbf{f}_i^{(k)}\|_2 = 1$.

The numerator of the loss function in Eq. (1) favors a similar representation for two augmented versions of the same data, while the denominator tries to increase the distance between each first augmented sample and the components of all other pairs. Note that, in practice, this loss is often symmetrized. For all the experiments in this work, the inverse temperature parameter is set to $\beta = 2$.

Rank estimation. The numerical estimation of the rank is based on the total variance explained as recently used to analyze the rank of DNNs embedding Daneshmand et al. (2020). For a given matrix W with singular values $\sigma_1, \dots, \sigma_d$ its estimated rank w.r.t to τ is defined as

$$\text{Rank}_\tau(W) = \sum_{j=1}^d 1_{\{|\sigma_j| \geq \tau\}}, \quad (2)$$

that is, it is the number of singular values whose absolute values are greater than τ .

3 An interpretable InfoNCE upper bound

In this section, we propose an upper bound on the InfoNCE loss that will allow us to derive insights into (i) the impact of the strength of the data augmentation policies on the projector and encoder embeddings and (ii) the nature of the information discarded by the projector and (iii) how does increasing the depth and width of the projector affect the encoder embedding. We provide an overview of InfoNCE in Appendix C. The following proposition illustrates the InfoNCE upper bound in the case of a linear projector.

Proposition 3.1. *Considering a linear projector $g(\mathbf{h}_i^{(k)}) = W^T \mathbf{h}_i^{(k)}$, $W \in \mathbb{R}^{d_{enc} \times d_{proj}}$, InfoNCE is upper bounded by*

$$\mathcal{L}_{\text{Upper}} = \beta \mathcal{L}_{\text{invariance}} + \beta \mathcal{L}_{\text{repulsion}} + \log(2(N-1)), \quad (3)$$

where

$$\mathcal{L}_{\text{invariance}} = -\frac{1}{N} \sum_{i=1}^N \text{Sim}(W^T \mathbf{h}_i^{(1)}, W^T \mathbf{h}_i^{(2)}), \quad (4)$$

$$\mathcal{L}_{\text{repulsion}} = \frac{1}{N} \sum_{i=1}^N \text{Sim}(W^T \mathbf{h}_i^{(1)}, W^T \tilde{\mathbf{h}}_i^*), \quad (5)$$

$\text{Sim}(\mathbf{x}, \mathbf{y}) = \mathbf{x}^T \mathbf{y} / (\|\mathbf{x}\| \|\mathbf{y}\|)$ and $\tilde{\mathbf{h}}_i^* = \arg \max_{\tilde{\mathbf{h}}_l, l \in B-i} \text{Sim}(W^T \mathbf{h}_i^{(1)^T}, W^T \tilde{\mathbf{h}}_l)$. (Proof in Appendix D.2).

While in the InfoNCE for each augmented sample the negative samples taken into account are within a ball of radius defined by β (Appendix C for detailed explanations), in our upper bound in Eq. (3), we only consider the negative sample resembling the most with its corresponding first augmented sample, denoted by $\tilde{\mathbf{h}}_i^*$.

The bound $\mathcal{L}_{\text{Upper}}$ of Eq. (3) captures the essential trade-offs in SSL: $\mathcal{L}_{\text{invariance}}$ corresponds to the maximization of the similarity between two versions of the same augmented data in the projector’s output space, while $\mathcal{L}_{\text{repulsion}}$ approximates the repulsion term that aims at suppressing the collapse of the representation by using the closest negative sample. In Fig. 3, we show that InfoNCE and $\mathcal{L}_{\text{Upper}}$ behave similarly during training. While tightening the bound seems possible, $\mathcal{L}_{\text{Upper}}$ is intuitive and sufficient to support our analysis.

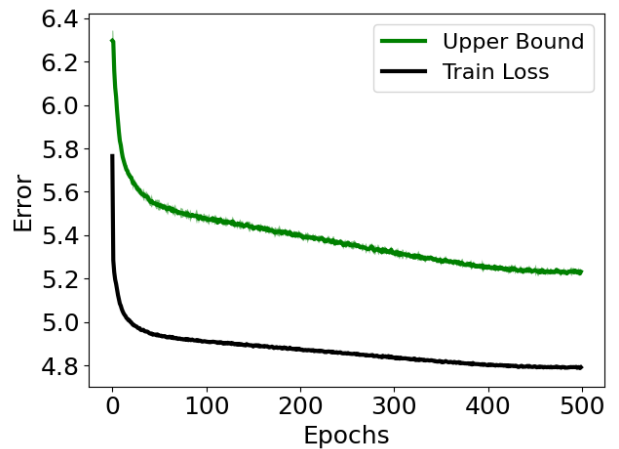


Figure 3: **The upper bound $\mathcal{L}_{\text{Upper}}$ in Eq. (3) tracks the InfoNCE loss** (mean and standard deviation over 5 runs) throughout training with a batch size of 128.

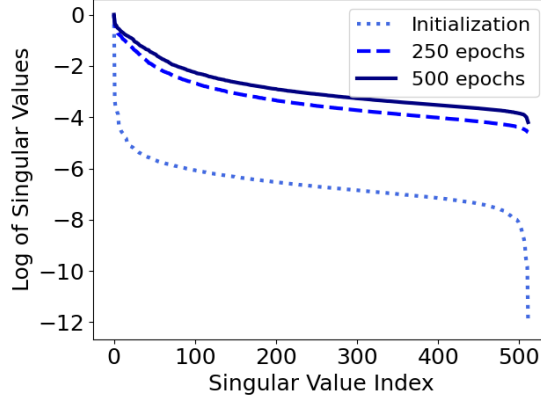


Figure 4: **Encoder space log-singular values** for Cifar100 dataset ($d_{\text{enc}} = 512$). The log-spectrum is evaluated at different training time: initialization (*dotted line*), half-training time (*dashed line*), and after training (*solid line*). In these three settings, the estimated rank (see Eq. (2)) leads to $\text{Rank}[\mathbf{h}_i^{(k)}, \dots, \mathbf{h}_i^{(k)}] \approx 512$, i.e., the embedded transformed samples span all the available directions in the encoder space (albeit a slight rank deficiency at initialization).

4 Dimensional collapse hinges on augmentations strength

In this section, we leverage the upper bound in Eq. (3) to show that the dimensional collapse of the projector network is directly related to the strength of the augmentation policies as well as the number of augmentations, as observed in Fig. 1. In particular, the stronger the augmentations, the lower the rank of the projector weights. We also show how the augmentations affect the distribution of the data in the encoder’s embedding. We first consider $\mathcal{L}_{\text{invariance}}$ and $\mathcal{L}_{\text{repulsion}}$ from Eq. (3) separately, before addressing their interaction. We provide in Fig. 2 a description of the interactions between the invariance term and repelling term with respect to the strength of the augmentations.

(1) The **invariance term** $\mathcal{L}_{\text{invariance}}$ in Eq. (4) promotes the augmented samples to coincide; we show here how it affects the rank of the projector weights and how stronger augmentations cause the projector mapping to be invariant. We first develop some intuitions by modeling the transformations as a linear action in the encoder space. While this approach can always be achieved as the output of the encoder defines a vector space, we will then show that modeling the augmentations as Lie group transformations will provide more insights.

(a) *Linear transformations in encoder space.* This additive relationship between augmented pair in the encoder space can be formally described by $\forall i, \mathbf{h}_i^{(2)} = \mathbf{h}_i^{(1)} + \mathbf{v}_i$, where $\mathbf{v}_i \in \mathbb{R}^{d_{\text{enc}}}$. Note that this formalism is always verified in practice. Following this approach, the invariance term can be re-written as

$$\mathcal{L}_{\text{invariance}} = \frac{1}{N} \sum_{i=1}^N -\text{Sim}(W^T \mathbf{h}_i^{(1)}, W^T (\mathbf{h}_i^{(1)} + \mathbf{v}_i)), \quad (6)$$

which can be minimized by maximizing the cosine similarity between $W^T \mathbf{h}_i^{(1)}$ and $W^T (\mathbf{h}_i^{(1)} + \mathbf{v}_i)$. This can be achieved by projector weights, i.e., W , such that: (i) $W^T \mathbf{v}_i$ is colinear to $W^T \mathbf{h}_i^{(1)}$ or (ii) the \mathbf{v}_i are in the null space of W . In both cases, the cosine similarity is maximized. This observation leads to the following proposition.

Proposition 4.1. *Assuming $\mathbf{h}_i^{(1)}$ and $\mathbf{h}_i^{(2)}$ are not colinear for all $i = 1, \dots, N$, then $\mathcal{L}_{\text{invariance}}$ is minimized if and only if $\mathbf{v}_i \in \text{Ker}(W)$. That is, the direction of augmentations in the encoder space belong to the kernel of the projector’s weights. (Proof in Appendix D.3)*

Therefore, by the rank-nullity theorem, the rank of the projector weights decreases as the dimension of the span of the direction of the augmentations increases, i.e., as $\text{Rank}(\mathbf{v}_1, \dots, \mathbf{v}_N)$ becomes large. Interestingly,

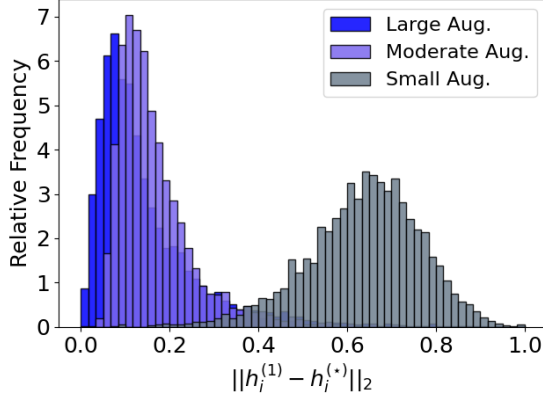


Figure 5: **Visualization of the normalized Euclidean distance between $\mathbf{h}_i^{(1)}$ and \mathbf{h}_i^*** for different training configurations: small, moderate, and large augmentations. Under large augmentations, the repulsion term $\mathcal{L}_{\text{repulsion}}$ is deemphasized. Under small augmentations, $\mathcal{L}_{\text{repulsion}}$ dominates the loss. The augmentation strength act as a per-datum scalar weight that governs how much the representation needs to be invariant as opposed to how much each augmented sample and their nearest neighbor should be projected onto opposite directions.

if all these augmented directions are mapped onto a low-dimensional subspace by the backbone encoder, then the rank of the projector weights can be maintained which is formalized by the following proposition.

Proposition 4.2. *The lower the rank of the subspace the encoder maps the augmented directions onto, the lower achievable dimensional collapse of the projector. (Proof in Appendix D.4).*

Intuitively, the dimension of the span of the \mathbf{v}_i ’s increases if augmentations point in different directions in the encoder space. Besides, the larger the spread (i.e., the difference between the maximum and minimum strength) of the augmentation policy distribution \mathcal{T} , the higher the dimension of the span of the \mathbf{v}_i . We provide empirical evidence regarding this aspect in Appendix E.

(b) *Non-linear transformations in encoder space.* We formalize non-linear transformations as the result of the application of Lie groups onto the data embedded in the encoder space. This is motivated by the fact that the encoder output is a continuous piecewise affine low dimensional manifold Ansuini et al. (2019); Balestrierio et al. (2019), in which the Lie group defines transformations between points that can model those observed in various natural datasets Connor et al. (2021); Cosentino et al. (2022).

Formally, $\mathbf{h}_i^{(2)} = \exp(\epsilon_i G) \mathbf{h}_i^{(1)}$, where $G \in \mathbb{R}^{d_{\text{enc}} \times d_{\text{enc}}}$ is the generator of a Lie group that characterizes the type of transformation and ϵ_i is a scalar denoting the strength of the transformations induced by G applied onto the i^{th} datum. A primer on Lie group transformations is provided in Appendix B. Note that in practice, the ϵ_i are the strength parameters that are sampled from the policy distribution and the type of transformation is defined by the selected augmentation policy, e.g., crop, colorjitter, horizontal flipping.

We can now express $\mathcal{L}_{\text{invariance}}$ as a function of the strength parameter as well as the generator of the transformation.

$$\mathcal{L}_{\text{invariance}} = -\frac{1}{N} \sum_{i=1}^N \text{Sim}(W^T \mathbf{h}_i^{(1)}, W^T \exp(\epsilon_i G) \mathbf{h}_i^{(1)}). \quad (7)$$

We observe that, (i) if the sampled strength ϵ_i is 0, then the similarity is maximized and therefore the invariance term does not penalize the loss function, and (ii) the larger the strength parameter is the more $\exp(\epsilon_i G) \mathbf{h}_i^{(1)}$ differs from $\mathbf{h}_i^{(1)}$ thus penalizing the loss function, except if the generator of the transformation, i.e., G , is in the kernel of W which we now discuss. Therefore, the strength of the augmentation acts as a balancing term between the invariance loss and the repulsion loss. In particular, the strength of the transformation corresponds to a per-datum scalar weight that governs how much the transformation affects the projector mapping toward an invariant representation, as depicted in Fig. 2.

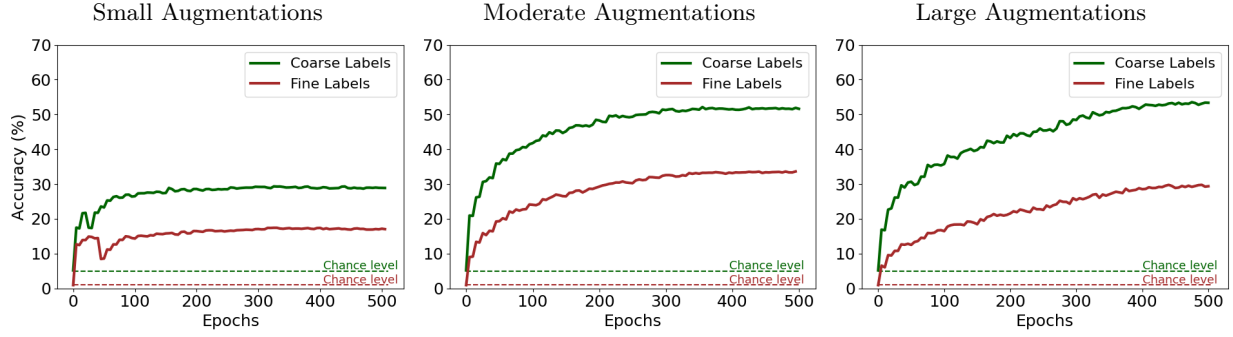


Figure 6: **Percentage of matching labels between \tilde{h}_i^* and $h_i^{(2)}$** for the 100 fine and 20 coarse labels of the Cifar100 dataset when training with different augmentation strengths. Recall that the index of \tilde{h}_i^* is determined in the projector’s output space as defined in Proposition 3.1. We observe that during training, across all augmentation regimes, the amount of shared semantic information increases. As the augmentation strength increases, the training time for the converge of this semantic sharing increases as well. Under small augmentations it converges after a couple hundred epochs, whereas under large augmentations it did not converge yet after 500 epochs. The strength of the augmentation establishes the trade-off between the invariance and repulsion terms (Sec. 4): under small small augmentations, the repulsion term dominates, which results in a poor representation of the data manifold.

The following proposition provides insights into the dimensional collapse of the projector and its relationship with the augmentation policy.

Proposition 4.3. *Assuming $h_i^{(1)}$ and $h_i^{(2)}$ are not colinear for all $i = 1, \dots, N$ then $\mathcal{L}_{invariance}$ is minimized if and only if $G \in \text{Ker}(W)$. That is, the generator of the augmentation policy belongs to the kernel of the projector’s weights. (Proof in Appendix D.5).*

This proposition shows that, in order to maximize the similarity, the projector weights, i.e., W , have to align its kernel with the generators underlying the augmentation policies. Note that we consider here only one group generator G while in practice one can be associated to each augmentation type. Thus, increasing the number of transformations will increase the dimension of the null space of W , except if their generator spans similar directions.

(2) We now consider the **repulsion term** $\mathcal{L}_{repulsion}$ in Eq. (5). This term is minimized if for each $i = 1, \dots, N$, we have $\text{Sim}(W^T h_i^{(1)}, W^T \tilde{h}_i^*) = -1$. That is, the angle between $W^T h_i^{(1)}$ and $W^T \tilde{h}_i^*$ is π . To do so, the projector maps $h_i^{(1)}$ and its nearest neighbor \tilde{h}_i^* onto diametrically opposed directions.

If it is feasible for the projector to map each $h_i^{(1)}$ and \tilde{h}_i^* onto diametrically opposed directions, the representation provided would not encapsulate any information regarding the data manifold. It is therefore necessary that the invariance term dominates the loss function to capture information regarding the data manifold. As we mentioned, the strength of the augmentation acts as a per-sample balancing term between the invariance term and the repulsion term. This enables us to understand why current practices in SSL consider the use of large augmentations.

In Fig. 5 we provide the histogram of the distances between $h_i^{(1)}$ and \tilde{h}_i^* . As we understood from the previous discussions, when the augmentations are small, this distance tends to be higher as the $\mathcal{L}_{repulsion}$ term has a greater impact than $\mathcal{L}_{invariance}$ on the InfoNCE loss. Conversely, for stronger augmentations, the $\mathcal{L}_{invariance}$ term dominates.

Note that, in this section, we assume that the linearization capability of the resnet with respect to the transformations enables us to express the transformations with respect to the the generator of the transformation and the per-sample strength. In practice, this linearization capability might be limited, and therefore, the projector mapping discards more than just the generator induced by the augmentation policies. This loss of information has been empirically observed in Chen et al. (2020b); Appalaraju et al. (2020).

5 Large augmentations and deep projector benefit encoder’s estimation of the data manifold

In the previous section we showed the relationship between the dimensional collapse of the projector, the number and strength of augmentations, and the distribution of the data in the encoder’s embedding. We now propose to analyze the relationship between the encoder and projector mappings through the lens of data manifold estimation and show how augmentations strength as well as architecture of the projector affect the quality of the encoder embedding. For sake of clarity, we first develop the case of linear projector, then, we resolve the case of non-linear projector.

We focus our analysis by considering the following reformulation of the upper bound in Eq. (3) with the assumption that the output of the projector are normalized

$$\mathcal{L}_{\text{Upper}} = \frac{1}{N} \sum_{i=1}^N -\beta \delta \mathbf{h}_i^T \text{Proj}(\mathbf{h}_i^{(1)}) + \log(2(N-1)), \quad (8)$$

with $\delta \mathbf{h}_i = \mathbf{h}_i^{(2)} - \tilde{\mathbf{h}}_i^*$ and where in the case of a linear projector

$$\text{Proj}(\mathbf{h}_i^{(1)}) = WW^T \mathbf{h}_i^{(1)}, \quad (9)$$

i.e., the projection of $\mathbf{h}_i^{(1)}$ onto the column space of W .

To minimize Eq. (8), W should enable the projection of $\mathbf{h}_i^{(1)}$ onto $\delta \mathbf{h}_i$. Therefore, the columns of W needs to include in their span $\mathcal{S} = \text{Span}\{\delta \mathbf{h}_i, i = 1, \dots, N\}$. We empirically verify this behaviour; specifically, in Fig. 7 we show that during training the fraction of variance of \mathcal{S} unexplained by W is decreasing, where the fraction of variance of \mathcal{S} unexplained by W is computed as follows

$$\sum_i \min_{t_i \in \mathbb{R}^{d_{\text{proj}}}} \|\delta \mathbf{h}_i - W t_i\|_2^2 / \sum_i \|\delta \mathbf{h}_i\|_2^2. \quad (10)$$

We posit that the remaining part of the unexplained variance is mainly due to the fact that (i) the encoder embedding of the $\delta \mathbf{h}_i$ is non-linear, (ii) the Resnet18 backbone encoder is not capable of linearizing \mathcal{S} . We now propose to characterize the subspace \mathcal{S} that appears to be crucial in determining the interplay between the projector and encoder mappings.

Noisy estimate of the data manifold tangent plane. We now consider the $\delta \mathbf{h}_i$ as displacement vectors that are the noisy estimate of a manifold tangent plane. This modelization of manifold tangent space has been commonly used in manifold estimation techniques, for more details the reader can refer to Tenenbaum et al. (2000); Bengio & Monperrus (2005); Bengio et al. (2005); Hashimoto et al. (2017). We are interested in knowing how close to the data manifold this estimated tangent space is and how the strength of the augmentation affects this estimation process. We depict in Fig. 6 the amount of label sharing between $\tilde{\mathbf{h}}_i^*$ and $\mathbf{h}_i^{(2)}$, as training progresses. Note that Cifar100 contains 100 fine and 20 coarse classes. We observe that the semantic similarity between $\mathbf{h}_i^{(2)}$ and $\tilde{\mathbf{h}}_i^*$ increases with the augmentation strength. Therefore, large augmentations make $\delta \mathbf{h}_i$ to be a close estimate of the data manifold tangent space.

This observation can be understood from the following reasoning: (i) In the large augmentations regime, at initialization, $\mathbf{h}_i^{(2)}$ and $\tilde{\mathbf{h}}_i^*$ are distant from each other (as $\tilde{\mathbf{h}}_i^*$ is near $\tilde{\mathbf{h}}_i^1$). Thus, the directions spanned by $\delta \mathbf{h}_i$ are a coarse estimation of the underlying data manifold. However, from Sec. 4, we know that during training, $\mathcal{L}_{\text{invariance}}$ dominates, so that $\mathbf{h}_i^{(2)}$ becomes closer to \mathbf{h}_i^* . Therefore, for large augmentations, the estimation of the data manifold tangent plane becomes finer as training progresses. This phenomenon is observed in Fig. 6, where the percentage of $\tilde{\mathbf{h}}_i^*$ sharing similar semantic content with $\mathbf{h}_i^{(2)}$ steadily increases during training. (ii) In the small augmentations regime, at initialization, $\mathbf{h}_i^{(2)}$ and $\tilde{\mathbf{h}}_i^*$ are close to each other, but do not share the same label. During training, the dissimilarity between $\tilde{\mathbf{h}}_i^*$ and $\mathbf{h}_i^{(1)}$ increases as $\mathcal{L}_{\text{repulsion}}$

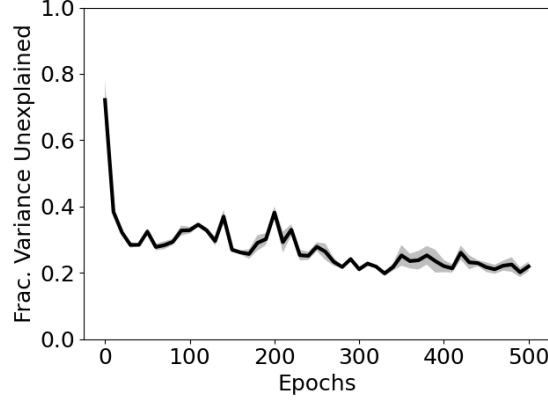


Figure 7: **Fraction of variance unexplained**, Eq. (10), as a measure of misalignment between the column space of the weights of the linear projector, i.e., W , and \mathcal{S} , where $\mathcal{S} = \text{Span}\{\delta\mathbf{h}_i, i = 1, \dots, N\}$ defined as (mean and standard deviation over 5 runs). We observe that the amount of unexplained variance decreases drastically after the initialization, showing that the projector attempts to approximate the subspace \mathcal{S} .

dominates the loss as discussed in Sec. 4 and observed in Fig. 6. The $\mathcal{L}_{\text{repulsion}}$ term of the loss does not favor specific directions. Therefore, it is hard to characterize how (the approximation of) the data manifold tangent plane in the encoder space evolves during training in the case of small augmentations.

Our geometrical understanding of the projector is displayed in Fig. 8 and can be summarized as follows: For each batch, one obtains in the encoder space an estimate of the data manifold directions by taking the difference between $\mathbf{h}_i^{(2)}$ and $\tilde{\mathbf{h}}_i^*$, then, the projector attempts to fit the subspace spanned by these vectors, defined as \mathcal{S} . Given the nature of this subspace, we conclude that the projector attempts to align each datum, embedded in the encoder space, onto the directions of the estimated data manifold tangent space. Therefore the projector discards the information that is not part of the subspace \mathcal{S} . From this, we understand that in the case of small augmentations, due to the proximity of $\mathbf{h}_i^{(1)}$, $\mathbf{h}_i^{(2)}$, and $\tilde{\mathbf{h}}_i^*$ at initialization, the error performed by the projector is small in order to obtain the desired projections. This also highlights why, in Fig. 1, the rank of the projector weights is not modified when training under small augmentations.

The effect of depth and width of non-linear projector. We now discuss how the width and depth of a non-linear projector affects its objective of projecting each $\mathbf{h}_i^{(1)}$ onto $\delta\mathbf{h}_i$. In particular, we show that when using an MLP, the approximation of \mathcal{S} is performed locally, i.e., each part of the encoder output space will be mapped by a different (local) affine transformation induced by the projector. Each affine transformation depends on both the type of non-linearity and the weights of the projector’s MLP. Therefore, the aforementioned discussions regarding the strength of the augmentations transfer to this case in a local manner.

We consider MLP projectors employing non-linearities such as (leaky-)ReLU, which are continuous piecewise affine operators. The particularity of these operators is that they induce a partition of their input space. In the present case, we consider the partition induced by the MLP projector, that is, of the output space of the encoder mapping. We will denote this partition as Ω of $\mathbb{R}^{d_{\text{enc}}}$. For more details regarding this approach considering the partitioning of DNN in their input space, the reader should refer to Balestrieri et al. (2018; 2019); Cosentino et al. (2020). Following this exact formulation, the projector mapping can now be expressed using the following closed-form (zeros-bias MLP projector is used for the sake of clarity)

$$g(\mathbf{h}_i^{(k)}) = \sum_{\omega \in \Omega} 1_{\{\mathbf{h}_i^{(k)} \in \omega\}} \left(W_{\omega}^T \mathbf{h}_i^{(k)} \right), \quad (11)$$

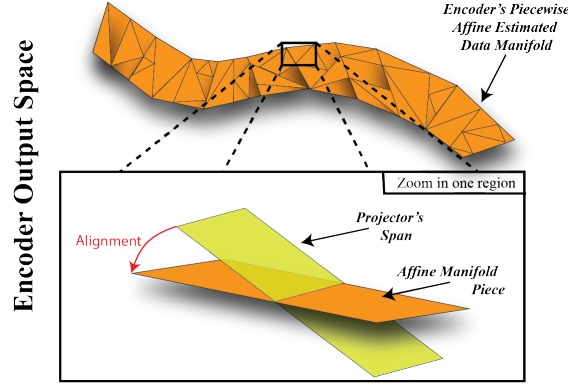


Figure 8: **Intuitive illustration of the projector aiming at aligning its column span with the noisy estimate of the data manifold tangent space performed by the encoder.** We provide here in the encoder output space the visualization of the noisy estimate of the data manifold: a continuous and piecewise affine surface representing \mathcal{S} (top). We shed light on the aim of the projector by zooming inside a region of this estimated manifold: it aligns the column span of its mapping (yellow) with the local estimated data manifold tangent space. In the case of a linear projector, the column of W should align with the entire estimated data manifold (top). Therefore forcing the encoder to provide a linear estimate of the data manifold. However, in the case of a non-linear projector, this alignment is performed locally. As the span of the projector is also a continuous and piecewise affine, using a non-linear projector lifts such a constraint on the encoder. The deeper and wider the projector is, the larger is its number of regions, therefore, the less constrained the encoder is with respect to its estimation of the data manifold tangent space. Note that our proposed analysis on the strength of the augmentations can be applied to the non-linear case by considering it locally, i.e., for each local affine map.

where Ω defines a partition of $\mathbb{R}^{d_{\text{enc}}}$, i.e., the encoder’s output. For each region $\omega \in \Omega$ in the encoder’s output space (as depicted by polytopes on top of Fig. 8), the projector acts as a linear mapping, induced by the weights W_ω .

It is now clear that whereas in the linear case the InfoNCE loss adjusts $\text{Proj}(\mathbf{h}_i^{(1)}) = WW^T \mathbf{h}_i^{(1)}$ to fit $\delta \mathbf{h}_i$, in the non-linear case, this fitting is performed locally; for each region ω in the encoder space, the corresponding W_ω is trained to fit the $\mathbf{h}_i^{(1)}$ samples belonging to the region ω onto the subspace \mathcal{S} . This is formally described as $\text{Proj}(\mathbf{h}_i^{(1)}) = \{W_\omega W_\omega^T \mathbf{h}_i^{(1)} | \mathbf{h}_i^{(1)} \in \omega\} \approx \delta \mathbf{h}_i$.

The deeper and wider the projector MLP is, the larger the number of regions ω and the smaller their volumes is Montúfar et al. (2021). Therefore, in the deep projector regime, the W_ω are trained to projector only one sample, $\mathbf{h}_i^{(1)}$, onto one estimate of the tangent space $\delta \mathbf{h}_i$. Thus, the granularity of the projection and the fitting of the displacement vector is getting more refined as the depth increases as the number of local mappings increases.

Therefore, while a linear projector forces the encoder to linearize the subspace \mathcal{S} , a non-linear projector can map this subspace to a non-linear manifold. The wider and deeper the non-linear projector’s MLP is, the less the encoder mapping is constrained. There is therefore a balance between not constraining at all the encoder and enabling it to unlock its expressive power. We now understand that the cross-validation observed regarding the architecture of the projector aimed at finding this balance. Our considerations allows us to understand why in Chen et al. (2020d), it was empirically shown that having deeper and larger MLPs could help to improve the accuracy of downstream tasks.

6 Related Work

We summarize in Table 6 the main differences with the related work. There are three key aspects differentiating this work. (a) **Encoder Analysis:** We provide both theoretical and empirical insights on the encoder

	DNN Mapping Insights		Data Augmentation Insights			
	Encoder Analysis	Projector Analysis	Theoretical Analysis	Empirical Analysis	Theoretical Aug. Model	Empirical Aug. Model
Our work	Yes	Linear\Nonlinear	Encoder	Encoder	Lie generator	Conv. practice
Jing et al. (2021)	No	Linear	Projector	Encoder	Additive noise	Gaussian noise
Huang et al. (2021)	No separate analysis		Projector	Encoder	(σ, δ) -augmentation	Conv. practice
Wang & Isola (2020)	No separate analysis		Projector	Encoder	-	Conv. practice
HaoChen et al. (2021)	No separate analysis		Projector	-	Gaussian noise	-
Tian et al. (2020)	No separate analysis		Projector	Encoder	-	Conv. practice
Wang & Liu (2021)	No separate analysis		-	Encoder	-	Conv. practice

embedding, i.e., the actual output used for downstream tasks. In contrast, the authors in Jing et al. (2021) do not analyze the learning in the encoding network. They investigate an end-to-end linear network that directly connects the input to the overall output fed to the loss function. Similarly, Wang & Isola (2020) analyzes theoretically an end-to-end network mapping the input to output living on the unit sphere and fed into the loss function. (b) **Nonlinear Projector**: Our analysis describes how a nonlinear projector impacts the encoder embedding and analyze the effect of its depth and width on the geometry of the encoder. (c) **Lie Group**: While existing approaches Jing et al. (2021); Huang et al. (2021); HaoChen et al. (2021) are distance-based, our provides a way to capture geometric information via the Lie generator

7 Conclusions

In this work, we have investigated the intricate relationship between the strength of the policy augmentations, the encoder representation, and the projector’s effective dimensionality in the context of contrastive self-supervised learning. Our analysis justifies the use of large augmentations in practice. Under small augmentations, the data representations are haphazardly mutually repulsed, leading them to reflect the semantics poorly. However, under large augmentations, SSL attempts to approximate the data manifold, extracting in the process useful representation for downstream transfer tasks. However, we also showed that large augmentations forces the projector mapping to discard a large amount of information to project each transformed data onto the estimate of the data manifold. Therefore, discarding the projector mapping for extracting data embedding is necessary as long as SSL requires large augmentations. Pursuit of more interpretable contrastive SSL without projector will require the development of a framework efficient in a small augmentations regime.

References

- Alessio Ansuini, Alessandro Laio, Jakob H. Macke, and Davide Zoccolan. Intrinsic dimension of data representations in deep neural networks. *CoRR*, abs/1905.12784, 2019. URL <http://arxiv.org/abs/1905.12784>.
- Srikar Appalaraju, Yi Zhu, Yusheng Xie, and István Fehérvári. Towards good practices in self-supervised representation learning, 2020.
- Randall Balestriero, Romain Cosentino, Behnaam Aazhang, and Richard Baraniuk. The geometry of deep networks: Power diagram subdivision. *Advances in Neural Information Processing Systems*, 32:15832–15841, 2019.
- Randall Balestriero et al. A spline theory of deep learning. In *International Conference on Machine Learning*, pp. 374–383. PMLR, 2018.
- Adrien Bardes, Jean Ponce, and Yann LeCun. Vicreg: Variance-invariance-covariance regularization for self-supervised learning. *CoRR*, abs/2105.04906, 2021. URL <https://arxiv.org/abs/2105.04906>.
- Yoshua Bengio and Martin Monperrus. Non-local manifold tangent learning. *Advances in Neural Information Processing Systems*, 17(1):129–136, 2005.

- Yoshua Bengio, Hugo Larochelle, and Pascal Vincent. Non-local manifold parzen windows. In *NIPS*, volume 18, pp. 115–122, 2005.
- Mathilde Caron, Piotr Bojanowski, Armand Joulin, and Matthijs Douze. Deep clustering for unsupervised learning of visual features. *CoRR*, abs/1807.05520, 2018. URL <http://arxiv.org/abs/1807.05520>.
- Mathilde Caron, Ishan Misra, Julien Mairal, Priya Goyal, Piotr Bojanowski, and Armand Joulin. Unsupervised learning of visual features by contrasting cluster assignments. *CoRR*, abs/2006.09882, 2020. URL <https://arxiv.org/abs/2006.09882>.
- Mathilde Caron, Hugo Touvron, Ishan Misra, Hervé Jégou, Julien Mairal, Piotr Bojanowski, and Armand Joulin. Emerging properties in self-supervised vision transformers. *CoRR*, abs/2104.14294, 2021. URL <https://arxiv.org/abs/2104.14294>.
- Ting Chen, Simon Kornblith, Mohammad Norouzi, and Geoffrey Hinton. A simple framework for contrastive learning of visual representations, 2020a.
- Ting Chen, Simon Kornblith, Mohammad Norouzi, and Geoffrey E. Hinton. A simple framework for contrastive learning of visual representations. *CoRR*, abs/2002.05709, 2020b. URL <https://arxiv.org/abs/2002.05709>.
- Ting Chen, Simon Kornblith, Kevin Swersky, Mohammad Norouzi, and Geoffrey Hinton. Big self-supervised models are strong semi-supervised learners. *arXiv preprint arXiv:2006.10029*, 2020c.
- Ting Chen, Simon Kornblith, Kevin Swersky, Mohammad Norouzi, and Geoffrey E. Hinton. Big self-supervised models are strong semi-supervised learners. *CoRR*, abs/2006.10029, 2020d. URL <https://arxiv.org/abs/2006.10029>.
- Marissa Connor, Gregory Canal, and Christopher Rozell. Variational autoencoder with learned latent structure. In *International Conference on Artificial Intelligence and Statistics*, pp. 2359–2367. PMLR, 2021.
- Romain Cosentino, Randall Balestriero, Richard G. Baraniuk, and Behnaam Aazhang. Provable finite data generalization with group autoencoder. *CoRR*, abs/2009.09525, 2020. URL <https://arxiv.org/abs/2009.09525>.
- Romain Cosentino, Randall Balestriero, Richard Baranuik, and Behnaam Aazhang. Deep autoencoders: From understanding to generalization guarantees. In Joan Bruna, Jan Hesthaven, and Lenka Zdeborova (eds.), *Proceedings of the 2nd Mathematical and Scientific Machine Learning Conference*, volume 145 of *Proceedings of Machine Learning Research*, pp. 197–222. PMLR, 16–19 Aug 2022. URL <https://proceedings.mlr.press/v145/cosentino22a.html>.
- Hadi Daneshmand, Jonas Kohler, Francis Bach, Thomas Hofmann, and Aurelien Lucchi. Batch normalization provably avoids ranks collapse for randomly initialised deep networks. In H. Larochelle, M. Ranzato, R. Hadsell, M. F. Balcan, and H. Lin (eds.), *Advances in Neural Information Processing Systems*, volume 33, pp. 18387–18398. Curran Associates, Inc., 2020. URL <https://proceedings.neurips.cc/paper/2020/file/d5ade38a2c9f6f073d69e1bc6b6e64c1-Paper.pdf>.
- Debidatta Dwibedi, Yusuf Aytar, Jonathan Tompson, Pierre Sermanet, and Andrew Zisserman. With a little help from my friends: Nearest-neighbor contrastive learning of visual representations. *CoRR*, abs/2104.14548, 2021a. URL <https://arxiv.org/abs/2104.14548>.
- Debidatta Dwibedi, Yusuf Aytar, Jonathan Tompson, Pierre Sermanet, and Andrew Zisserman. With a little help from my friends: Nearest-neighbor contrastive learning of visual representations, 2021b.
- Linus Ericsson, Henry Gouk, and Timothy M. Hospedales. How well do self-supervised models transfer? *CoRR*, abs/2011.13377, 2020. URL <https://arxiv.org/abs/2011.13377>.

- Jean-Bastien Grill, Florian Strub, Florent Altché, Corentin Tallec, Pierre H. Richemond, Elena Buchatskaya, Carl Doersch, Bernardo Ávila Pires, Zhaohan Daniel Guo, Mohammad Gheshlaghi Azar, Bilal Piot, Koray Kavukcuoglu, Rémi Munos, and Michal Valko. Bootstrap your own latent: A new approach to self-supervised learning. *CoRR*, abs/2006.07733, 2020. URL <https://arxiv.org/abs/2006.07733>.
- B. Hall. *Lie Groups, Lie Algebras, and Representations: an Elementary Introduction*, volume 222. Springer, 2015.
- Jeff Z HaoChen, Colin Wei, Adrien Gaidon, and Tengyu Ma. Provable guarantees for self-supervised deep learning with spectral contrastive loss. *Advances in Neural Information Processing Systems*, 34, 2021.
- Tatsunori B Hashimoto, Percy S Liang, and John C Duchi. Unsupervised transformation learning via convex relaxations. In I. Guyon, U. V. Luxburg, S. Bengio, H. Wallach, R. Fergus, S. Vishwanathan, and R. Garnett (eds.), *Advances in Neural Information Processing Systems*, volume 30. Curran Associates, Inc., 2017. URL <https://proceedings.neurips.cc/paper/2017/file/86a1793f65aeef4aeef4b479fc9b2bca-Paper.pdf>.
- Kaiming He, Haoqi Fan, Yuxin Wu, Saining Xie, and Ross Girshick. Momentum contrast for unsupervised visual representation learning, 2020.
- Weiran Huang, Mingyang Yi, and Xuyang Zhao. Towards the generalization of contrastive self-supervised learning. *arXiv preprint arXiv:2111.00743*, 2021.
- Li Jing, Pascal Vincent, Yann LeCun, and Yuandong Tian. Understanding dimensional collapse in contrastive self-supervised learning. *CoRR*, abs/2110.09348, 2021. URL <https://arxiv.org/abs/2110.09348>.
- Alex Krizhevsky, Geoffrey Hinton, et al. Learning multiple layers of features from tiny images. *Citeseer*, 2009.
- Junnan Li, Pan Zhou, Caiming Xiong, Richard Socher, and Steven C. H. Hoi. Prototypical contrastive learning of unsupervised representations. *CoRR*, abs/2005.04966, 2020. URL <https://arxiv.org/abs/2005.04966>.
- Ishan Misra and Laurens van der Maaten. Self-supervised learning of pretext-invariant representations. *CoRR*, abs/1912.01991, 2019a. URL <http://arxiv.org/abs/1912.01991>.
- Ishan Misra and Laurens van der Maaten. Self-supervised learning of pretext-invariant representations, 2019b.
- Guido Montúfar, Yue Ren, and Leon Zhang. Sharp bounds for the number of regions of maxout networks and vertices of minkowski sums, 2021.
- Joshua B Tenenbaum, Vin De Silva, and John C Langford. A global geometric framework for nonlinear dimensionality reduction. *science*, 290(5500):2319–2323, 2000.
- Yonglong Tian, Chen Sun, Ben Poole, Dilip Krishnan, Cordelia Schmid, and Phillip Isola. What makes for good views for contrastive learning. *CoRR*, abs/2005.10243, 2020. URL <https://arxiv.org/abs/2005.10243>.
- Yuandong Tian, Xinlei Chen, and Surya Ganguli. Understanding self-supervised learning dynamics without contrastive pairs. In *International Conference on Machine Learning*, pp. 10268–10278. PMLR, 2021.
- Aaron van den Oord, Yazhe Li, and Oriol Vinyals. Representation learning with contrastive predictive coding, 2019.
- Feng Wang and Huaping Liu. Understanding the behaviour of contrastive loss. In *Proceedings of the IEEE/CVF conference on computer vision and pattern recognition*, pp. 2495–2504, 2021.
- Tongzhou Wang and Phillip Isola. Understanding contrastive representation learning through alignment and uniformity on the hypersphere. *CoRR*, abs/2005.10242, 2020. URL <https://arxiv.org/abs/2005.10242>.
- Chun-Hsiao Yeh, Cheng-Yao Hong, Yen-Chi Hsu, Tyng-Luh Liu, Yubei Chen, and Yann LeCun. Decoupled contrastive learning. *arXiv preprint arXiv:2110.06848*, 2021.

Yang You, Igor Gitman, and Boris Ginsburg. Large batch training of convolutional networks. *arXiv preprint arXiv:1708.03888*, 2017.

Jure Zbontar, Li Jing, Ishan Misra, Yann LeCun, and Stéphane Deny. Barlow twins: Self-supervised learning via redundancy reduction. *CoRR*, abs/2103.03230, 2021. URL <https://arxiv.org/abs/2103.03230>.

A Appendix

B Lie Group

A Lie group is a group that is a differentiable manifold. For instance, the group of rotation $SO(2) = \left\{ \begin{pmatrix} \cos(\theta) & -\sin(\theta) \\ \sin(\theta) & \cos(\theta) \end{pmatrix} \mid \theta \in \mathbb{R}/2\pi\mathbb{Z} \right\}$.

One of the main advantage of having a group with a differentiable manifold structure is that it can be defined by an exponential map: $SO(2) = \left\{ \exp(\theta G) \mid \begin{pmatrix} 0 & -1 \\ 1 & 0 \end{pmatrix}, \theta \in \mathbb{R}/2\pi\mathbb{Z} \right\}$, where G is the infinitesimal operator of the group. The infinitesimal operator G is thus encapsulating the group information.

The group action, defined as $g_\epsilon \cdot x = \exp(\epsilon G)x$, that is, $\exp(\epsilon G)$ corresponds to the mapping induced by the action of the group element g_ϵ onto the data x .

One can exploit the Taylor series expansion of the exponential map to obtain its linearized version

$$g \cdot x = \exp(\epsilon G)x \approx (I + \epsilon G)x \quad (12)$$

where x is the data and $\exp(\epsilon G)x$ its transformed version with respect to the group induced by the generator G . For more details regarding Lie group and the exponential map refer to Hall (2015).

C The InfoNCE Framework

We begin our analysis by considering the InfoNCE loss function, this loss function is commonly used in contrastive learning frameworks and has the benefit of providing multiple equivalent formulations that ease the derivation of insights regarding self-supervised learning embedding. In this section, we propose first a novel formulation of the InfoNCE which allows us to formalize common intuitions regarding contrastive learning losses. We then leverage this reformulation to provide an upper bound of the InfoNCE loss that will be central to our analysis regarding the role and properties of the projector. W.l.o.g. the proof will be first derived with $\|f_i^{(k)}\| = 1$ to not introduce further notations.

The following proposition is a re-expression of the InfoNCE that allows us to consider this loss function as a regularized non-contrastive loss function where the regularizations provides insights into how this loss is actually behaving.

Proposition C.1. *The infoNCE can be reformulated as*

$$\mathcal{L}_{\text{infoNCE}} = \frac{1}{N} \sum_{i=1}^N \left(-\beta f_i^{(1)T} f_i^{(2)} - \beta f_i^{(1)T} \mathbb{E}_{\mathcal{D}_{-i}}[\tilde{f}] + H(\mathcal{D}_{-i}) \right) \quad (13)$$

where, H denotes the entropy, \mathcal{D}_{-i} is a probability distribution such that $p_{\mathcal{D}_{-i}}(\tilde{f}_l; \beta) = \frac{\exp(\beta f_i^{(1)T} \tilde{f}_l)}{\sum_{k \in B_{-i}} \exp(\beta f_i^{(1)T} \tilde{f}_k)}$

and recall that $\{\tilde{f}_l : l \in B_{-i}\} = \{f_j^{(k)} : j \neq i, k = 1, 2\}$ (Proof in App.D.1).

When minimizing Eq. 13, the first term forces the two augmented data in the projector space to be as similar as possible, which is the intuition behind most self-supervised learning losses. Note that only relying on such a similarity loss often leads to the collapse of the representation, that is one issue that is tackled in non-contrastive self-supervised learning using various hacks Caron et al. (2020); Grill et al. (2020).

How InfoNCE selects its negative pairs? From Proposition C.1, we observe that, when training under the InfoNCE, two additional terms act as a regularization to this non-contrastive similarity loss function, hindering the representation’s collapse. In particular, the second term, $\beta f_i^{(1)T} \mathbb{E}_{\mathcal{D}_{-i}}[\tilde{f}]$, pushes the first augmented data in the projector space to be as different as possible to a weighted average of the other data. This expectation is dependant on the probability distribution \mathcal{D}_{-i} , which assigns high probability to data that are similar to $f_i^{(1)}$. Thus, the more the $f_i^{(1)}$ resembles \tilde{f}_l , the more they account for the loss, and hence the more they tend to be repelled. Now, it is clear that if the distribution \mathcal{D}_{-i} is uniform, then all the data will tend to account for the same error. The third term avoids this by forcing this distribution to be with local support, and therefore, only consider a few instances of \tilde{f}_l , in particular, the ones that are the most similar to $f_i^{(1)}$. This last term thus enforces the \tilde{f}_l to be different from each other by being repelled with different strength from $f_i^{(1)}$.

How does the temperature parameter affects these regularizations? From the Proposition C.1, we develop some understanding regarding the temperature parameter β ; in particular, this parameter influences the distribution \mathcal{D}_{-i} , which in turn, characterizes how local or global is the data taken into account into the repulsion process allowing to the differentiation between every data embedding. We first observe that, when $\beta \rightarrow +\infty$, $\mathbb{E}_{\mathcal{D}_{-i}}[\tilde{f}] = \arg \max_{\tilde{f}_l, l \in B_{-i}} f_i^{(1)T} \tilde{f}_l$, which induces that only the closest data from $f_i^{(1)}$ that is not $f_i^{(2)}$ is taken into account in the error. Besides, when $\beta \rightarrow 0$, $H(\mathcal{D}_{-i}) \rightarrow 0$, therefore, this regularization term does not affect the loss function. This shows that increasing the temperature parameter reduces the support of the candidates for negative pairs and that the ones considered are the ones most similar to the considered data. Therefore, the temperature parameter effects the support of the per data distribution underlying the regularisation terms, $f_i^{(1)T} \mathbb{E}_{\mathcal{D}_{-i}}[\tilde{f}]$ and $H(\mathcal{D}_{-i})$. From this, it is clear that having only one temperature parameter for the entire dataset is not adequate, as the locality of the distribution should be aligned with the volume of the data required to be repelled.

D Proofs

D.1 Proposition C.1

Proof.

$$\mathcal{L}_{\text{infoNCE}} = -\frac{1}{N} \sum_{i=1}^N \log\left(\frac{\exp(\beta f_i^{(1)T} f_i^{(2)})}{\sum_{l \in B_{-i}} \exp(\beta f_i^{(1)T} \tilde{f}_l)}\right). \quad (14)$$

Let’s denote by $Z_i = \sum_{l \in B_{-i}} \exp(\beta f_i^{(1)T} \tilde{f}_l)$ and let’s consider the loss function for each data i denoted by $l_i = -\log\left(\frac{\exp(\beta f_i^{(1)T} f_i^{(2)})}{Z_i}\right)$.

Let’s now define \mathcal{D}_{-i} a probability distribution such that $p_{\mathcal{D}_{-i}}(\tilde{f}_l; \beta) = \frac{\exp(\beta f_i^{(1)T} \tilde{f}_l)}{Z_i}$.

We then compute the entropy of such distribution,

$$\begin{aligned} H(\mathcal{D}_{-i}) &= \sum_{l \in B_{-i}} p_{\mathcal{D}_{-i}}(\tilde{f}_l; \beta) \log\left(\frac{1}{p_{\mathcal{D}_{-i}}(\tilde{f}_l; \beta)}\right) \\ &= \log(Z_i) - \beta \sum_{l \in B_{-i}} p_{\mathcal{D}_{-i}}(\tilde{f}_l; \beta) f_i^{(1)T} \tilde{f}_l \\ &= \log(Z_i) - \beta f_i^{(1)T} \mathbb{E}_{\mathcal{D}_{-i}}[\tilde{f}]. \end{aligned} \quad (15)$$

Thus, $\log(Z_i) = H(\mathcal{D}_{-i}) + \beta f_i^{(1)T} \mathbb{E}_{\mathcal{D}_{-i}}[\tilde{f}]$.

From $l_i = \log(Z_i) - \beta f_i^{(1)^T} f_i^{(2)}$ we obtain

$$l_i = -\beta f_i^{(1)^T} (f_i^{(2)} - \mathbb{E}_{\mathcal{D}_{-i}}[\tilde{f}]) + H(\mathcal{D}_{-i}).$$

Averaging over the $i = 1, \dots, N$ concludes the proof. \square

D.2 Proposition 3.1

Proof. We consider the result of Proposition C.1 and we take the derivative of Z_i (described in Proof D.1) with respect to β ,

$$\begin{aligned} \frac{\delta}{\delta\beta} \log(Z_i) &= \frac{\sum_{l \in B_{-i}} f^{(1)^T} \tilde{f}_l \exp(\beta f^{(1)^T} \tilde{f}_l)}{\sum_{l \in B_{-i}} \exp(\beta f^{(1)^T} \tilde{f}_l)} \\ &= f^{(1)^T} \frac{\sum_{l \in B_{-i}} \tilde{f}_l \exp(\beta f^{(1)^T} \tilde{f}_l)}{\sum_{l \in B_{-i}} \exp(\beta f^{(1)^T} \tilde{f}_l)} \\ &= f^{(1)^T} \mathbb{E}_{\mathcal{D}_{-i}}[\tilde{f}]. \end{aligned} \tag{16}$$

Then,

$$\log(Z_i|_{\beta'=\beta}) - \log(Z_i|_{\beta'=0}) = f_i^{(1)^T} \int_0^\beta \mathbb{E}_{\mathcal{D}_{-i}}[\tilde{f}] d\beta'.$$

Now, given that $Z_i|_{\beta'=0} = \sum_{l \in B_{-i}} 1 = 2(N-1)$, we have

$$\log(Z_i|_{\beta'=\beta}) = f_i^{(1)^T} \int_0^\beta \mathbb{E}_{\mathcal{D}_{-i}}[\tilde{f}] d\beta' + \log(2(N-1)).$$

Therefore,

$$l_i = -f_i^{(1)^T} \int_0^\beta (f_i^{(2)} - \mathbb{E}_{\mathcal{D}_{-i}}[\tilde{f}]) d\beta' + \log(2(N-1))$$

Now, defining $\mathbb{E}_\beta[\mathbb{E}_{\mathcal{D}_{-i}}[\tilde{f}]] = \frac{1}{\beta} \int_0^\beta \mathbb{E}_{\mathcal{D}_{-i}(\beta')}[\tilde{f}] d\beta'$, we have

$$\begin{aligned} l_i &= -\beta f_i^{(1)^T} (f_i^{(2)} - \mathbb{E}_\beta[\mathbb{E}_{\mathcal{D}_{-i}}[\tilde{f}]] + \log(2(N-1))) \\ &= -\beta f_i^{(1)^T} f_i^{(2)} + \beta \mathbb{E}_\beta[f_i^{(1)^T} \mathbb{E}_{\mathcal{D}_{-i}}[\tilde{f}]] + \log(2(N-1)) \\ &\leq -\beta f_i^{(1)^T} f_i^{(2)} + \beta \mathbb{E}_\beta[f_i^{(1)^T} \tilde{f}_i^*] + \log(2(N-1)) \\ &= -\beta f_i^{(1)^T} f_i^{(2)} + \beta \frac{1}{\beta} \int_0^\beta f^{(1)^T} \tilde{f}_i^* d\beta' + \log(2(N-1)) \\ &= -\beta f_i^{(1)^T} f_i^{(2)} + \beta f^{(1)^T} \tilde{f}_i^* + \log(2(N-1)) \\ &= -\beta (f_i^{(1)^T} (f_i^{(2)} - \tilde{f}_i^*)) + \log(2(N-1)). \end{aligned} \tag{17}$$

Now, recall that recall that for sake of clarity we used $\|f_i^{(k)}\|_2 = 1$. Adding the normalization and assuming a linear projector, i.e., $g(h_i^{(k)}) = W^T h_i^{(k)}$ with $W \in \mathbb{R}^{d_{enc} \times d_{proj}}$ we obtain

$$l_i = -\beta \frac{h_i^{(1)^T} W W^T h_i^{(2)}}{\|W^T h_i^{(1)}\| \|W^T h_i^{(2)}\|} + \beta \frac{h_i^{(1)^T} W W^T \tilde{h}_i^*}{\|W^T h_i^{(1)}\| \|W^T \tilde{h}_i^*\|} + \log(2(N-1)) \tag{18}$$

Averaging over the $i = 1, \dots, N$ concludes the proof. \square

D.3 Proposition 4.1

Proof.

$$\mathcal{L}_{\text{invariance}} = \frac{1}{N} \sum_{i=1}^N -\text{Sim}(W^T \mathbf{h}_i^{(1)}, W^T(\mathbf{h}_i^{(1)} + \mathbf{v}_i))$$

is minimized if and only if $\forall i = 1, \dots, N$, $\cos(\theta_{\mathbf{h}_i^{(1)}, \mathbf{h}_i^{(1)} + \mathbf{v}_i}) = 1$, where $\theta_{\mathbf{h}_i^{(1)}, \mathbf{h}_i^{(1)} + \mathbf{v}_i}$ defines the angle between $W^T \mathbf{h}_i^{(1)}$ and $W^T(\mathbf{h}_i^{(1)} + \mathbf{v}_i)$. Denoting by \propto the signed colinearity operator, we have

$$\cos(\theta_{\mathbf{h}_i^{(1)}, \mathbf{h}_i^{(1)} + \mathbf{v}_i}) = 1 \quad (19)$$

$$\iff \theta_{\mathbf{h}_i^{(1)}, \mathbf{h}_i^{(1)} + \mathbf{v}_i} = 0 \quad (20)$$

$$\iff W^T \mathbf{h}_i^{(1)} \propto W^T(\mathbf{h}_i^{(1)} + \mathbf{v}_i) \quad (21)$$

$$\iff W^T \mathbf{v}_i = 0 \text{ or } W^T \mathbf{h}_i^{(1)} \propto W^T \mathbf{v}_i \quad (22)$$

$$\iff W^T \mathbf{v}_i = 0 \text{ or } W^T \mathbf{h}_i^{(1)} \propto W^T(\mathbf{h}_i^{(2)} - \mathbf{h}_i^{(1)}) \quad (23)$$

Since, $\mathbf{h}_i^{(1)}$ is not colinear with $\mathbf{h}_i^{(2)}$, we obtain

$$\iff W^T \mathbf{v}_i = 0. \quad (24)$$

Therefore, $\mathbf{v}_i \in \text{Ker}(W)$. □

D.4 Proposition 4.2

Proof. We have that $\text{Dim}(W) = \text{Nullity}(W) + \text{Rank}(W)$. Leveraging Proposition 4.1, we know that a projector minimizing $\mathcal{L}_{\text{invariance}}$ has the following property, $\text{Nullity}(W) \geq \text{Dim}(\text{Rank}(\mathbf{v}_1, \dots, \mathbf{v}_N))$. As $(\mathbf{v}_1, \dots, \mathbf{v}_N)$ is defined as the augmentation direction of the input manifold in the backbone encoder, it is clear that their rank is defined by the dimension of the subspace the encoder project the augmented directions. □

D.5 Proposition 4.3

Proof. A commonly used tool in the analysis of manifold induced by Lie group is the linearization of the exponential map. This exhibits the Lie algebra of the group, that is, a vector space to which the generator belongs (some details for in Appendix B). We follow this approach and consider the linearized exponential map leading to

$$\mathcal{L}_{\text{invariance}} = -\frac{1}{N} \sum_{i=1}^N \text{Sim}(W^T \mathbf{h}_i^{(1)}, W^T(\mathbf{h}_i^{(1)} + \epsilon_i G \mathbf{h}_i^{(1)})). \quad (25)$$

Following the proof in Appendix D.3, we obtain that $\mathcal{L}_{\text{invariance}}$ is minimized if and only if $\text{Col}(G) \in \text{Ker}(W)$, where $\text{Col}(G)$ denotes the columns of the generator G . Note that, if we lift the linearization and keep higher order term in the exponential map, we obtain that the powers of G should be in the kernel of W . □

E Toy-example - Rank versus Augmentation Strength

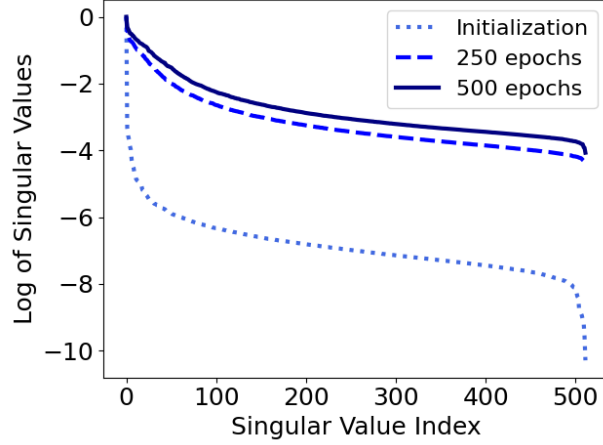


Figure 9: Encoder space log-singular values for the transformed Cifar100 dataset where the encoder space dimension = 512 and a linear projector of output dimension = 128. The log-spectrum is evaluated at different training time: initialization (*dotted line*), half-training time (*dashed line*), and after training (*solid line*). In these three settings, the calculation of the rank following Eq. 2, leads to $\text{Rank}_\tau [h^{(1)}(x_1), \dots, h^{(1)}(x_N)] = 512$, that is, the representation induced by the encoder is full rank (and close to full rank at the initialization) until the end of the training as for the case where the input data are not transformed, in Fig. 4.

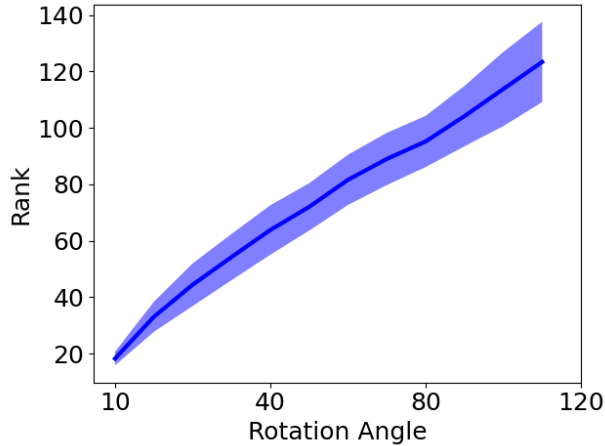


Figure 10: **Rank of the covariance matrix of 500 rotated version of a random one-hot image** of dimension 32×32 (mean and standard deviation for 5 runs). We sample the angle between 0 and the x -axis angle value uniformly. The larger the transformation, the higher rank the collection of images is, and there the lower rank a linear map is required to provide an invariant map to this specific transformation